PNAS INAUGURAL ARTICLE | EARTH, ATMOSPHERIC, AND PLANETARY SCIENCES

Lithium isotope evidence for a plumeworld ocean in the aftermath of the Marinoan snowball Earth

Tian Gan[a,b,c,d], Meng Tian[e,f,1], Xi-Kai Wang[g], Shijie Wang[a], Xiao-Ming Liu[g,1], Ganqing Jiang[h], Benjamin C. Gill[b], Morrison Nolan[i], Alan J. Kaufman[c,j], Taiyi Luo[k], and Shuhai Xiao[b,1]

Affiliations are included on p. 10.

This contribution is part of the special series of Inaugural Articles by members of the National Academy of Sciences elected in 2023.
Contributed by Shuhai Xiao; received April 19, 2024; accepted September 25, 2024; reviewed by Mathieu Dellinger and Graham A. Shields

The snowball Earth hypothesis predicts that continental chemical weathering diminished substantially during, but rebounded strongly after, the Marinoan ice age some 635 Mya. Defrosting the planet would result in a plume of fresh glacial meltwater with a different chemical composition from underlying hypersaline seawater, generating both vertical and lateral salinity gradients. Here, we test the plumeworld hypothesis using lithium isotope compositions in the Ediacaran Doushantuo cap dolostone that accumulated in the aftermath of the Marinoan snowball Earth along a proximal–distal (nearshore–offshore) transect in South China. Our data show an overall decreasing δ^7Li trend with distance from the shoreline, consistent with the variable mixing of a meltwater plume with high δ^7Li (due to incongruent silicate weathering on the continent) and hypersaline seawater with low δ^7Li (due to synglacial distillation). The evolution of low δ^7Li of synglacial seawater, as opposed to the modern oceans with high δ^7Li, was likely driven by weak continental chemical weathering coupled with strong reverse weathering on the seafloor underneath silica-rich oceans. The spatial pattern of δ^7Li is also consistent with the development and then collapse of the meltwater plume that occurred at the time scale of cap dolostone accumulation. Therefore, the δ^7Li data are consistent with the plumeworld hypothesis, considerably reduced chemical weathering on the continent during the Marinoan snowball Earth, and enhanced reverse weathering on the seafloor of Precambrian oceans.

cryogenian period | plumeworld model | lithium isotopes | continental weathering | reverse weathering

Significance

It has been hypothesized that the surface ocean was frozen for several million years during an ice age known as the Marinoan snowball Earth. When this event ended ~635 Mya, a plumeworld ocean developed, with buoyant meltwater sitting above denser hypersaline seawater that aged during the glaciation. We use lithium isotopes (δ^7Li) to test the plumeworld scenario, noting that δ^7Li signatures would be different between meltwater and hypersaline seawater, with the former leaving a stronger fingerprint in rocks deposited nearshore than those in offshore environments. Our data are consistent with the plumeworld scenario and further reveal low δ^7Li values of the hypersaline seawater, likely due to muted continental weathering but strong seafloor reverse weathering during the snowball Earth.

The Neoproterozoic snowball Earth events represent extreme climate conditions that provide information about the limits of climate change on our planet (1). The best studied example is the terminal Cryogenian Marinoan glaciation that occurred ca. 650 to 635 Ma, with its termination marked by the global deposition of fine-grained cap dolostones (1–4). Multiple hypotheses have been proposed to account for the source of alkalinity for cap dolostone deposition, which may have derived from continental weathering (5, 6), gas hydrate destabilization and oxidation (7, 8), or oceanic overturn of alkalinity-rich deep waters (9). Quantitative calculations indicate that continental weathering was likely the primary source (10, 11) because alkalinity from deep seawater or gas hydrate destabilization was insufficient and failed to account for the globally ubiquitous deposition of the cap dolostone (11). During the Marinoan snowball Earth, the hydrological cycle, and hence continental chemical weathering, was greatly reduced (1). However, immediately after the Marinoan snowball Earth, continental weathering resumed strongly, with rapid deglaciation resulting in a plumeworld ocean (11), in which buoyant low-salinity meltwater persistently overlaid denser hypersaline seawater. The plumeworld ocean plausibly developed in two steps: first, thick sea ice would melt with increasing temperature, resulting in a vertically stratified ocean with a surface layer of freshwater above hypersaline seawater; second, the melting of continental glaciers would further enhance the vertical stratification and also dynamically maintain a nearshore–offshore (or proximal–distal) lateral gradient. The combined vertical and lateral gradients, along with the temporal sequence of the development and eventual collapse of the plumeworld ocean, would result in both spatial and stratigraphic patterns recorded in the cap dolostone. Indeed, stratigraphic changes in Sr, Mg, and Ca isotopes of Ediacaran cap dolostones deposited in the aftermath of the Marinoan snowball Earth revealed three stages in cap dolostone deposition, with the middle stage (stage II) characterized by a large positive excursion in both ^{87}Sr/^{86}Sr and δ^{26}Mg coupled with a negative excursion in δ^{44}Ca (12, 13). These isotopic anomalies suggest a strong

Reviewers: M.D., Environnements Dynamiques et Territoires de la Montagne; and G.A.S., University College London.

The authors declare no competing interest.

[1] To whom correspondence may be addressed. Email: meng.tian@physik.lmu.de, xiaomliu@email.unc.edu, or xiao@vt.edu.

This article contains supporting information online at https://www.pnas.org/lookup/suppl/doi:10.1073/pnas.2407419121/-/DCSupplemental.

influx of terrestrial meltwater with a continental source of radiogenic Sr, heavy Mg isotopes, and light Ca isotopes during Stage II. In contrast, in the early and late stages of cap dolostone deposition (stages I and III), geochemical signal for continental influx is weaker, presumably related to initial sea ice melting (stage I) and eventual collapse of the plumeworld ocean (stage III). Boron isotopes are also consistent with rapid changes in the pH of postglacial seawater (12, 14), possibly associated with variable mixing of freshwater with low pH and hypersaline marine water with high pH. A recent box model based on δ^{26}Mg balance (13) and an energy model based on turbulent mixing (15, 16) further estimated a timescale of ~10^3 to 10^4 y for the persistence of the plume before it is fully mixed with seawater.

The above-cited studies largely focused on chemostratigraphic patterns to reveal the succession of events over the time period when the cap dolostone was deposited. Few studies have explored the spatial patterns of isotopic systems from multiple cap dolostone sections in the same sedimentary basin. Because the plumeworld hypothesis makes predictions about vertical oceanic stratification and lateral nearshore–offshore gradients, as well as a temporal sequence of events, it is important to analyze spatial variations in cap dolostone geochemistry. Here, we independently test the plumeworld hypothesis using Li isotope data of the Doushantuo cap dolostone in South China, from multiple sections representing a nearshore–offshore transect of the sedimentary basin. The geochemical data are supplemented by numerical modeling to illuminate the intensity of synglacial isotopic distillation and postglacial mixing of the oceans.

The geochemical cycle of lithium in modern oceans is generally well understood (17, 18). Because of their substantial mass difference (~17%), ^{6}Li and ^{7}Li fractionate strongly during mineral-fluid interactions (18). Importantly, the fractionation factors are largely constant, with negligible dependence on temperature, salinity, Li/Ca ratios, biological processes, and redox conditions (19–22). In the modern ocean, the two primary Li sources are riverine flux (1.0×10^{10} mol/y) derived from continental silicate weathering with an average δ^7Li of ~23‰ and marine hydrothermal flux (1.3×10^{10} mol/yr) with an average δ^7Li of 8.3‰ (23). The two major sinks are authigenic clay formation associated with silicate reverse weathering and low-temperature basalt alteration (24, 25). The δ^7Li isotopic offset between the river and upper continental crust is primarily influenced by weathering congruency. Incongruent continental weathering of silicates causes the preferential uptake of ^{6}Li into secondary clay minerals, resulting in the riverine δ^7Li much higher than the average continental crust, while congruent continental weathering results in relatively little isotopic preference during the dissolution of source silicate bedrocks, leading to a riverine input with bedrock-like δ^7Li values (26). As ^{6}Li is preferentially partitioned into clays during mineral–fluid interactions on the seafloor (i.e., reverse weathering) (22), δ^7Li of modern seawater (~31‰) is higher than that of average riverine input. Additionally, since the residence time of lithium in modern oceans is 0.3 to 1.5 Myr (27), much longer than the oceanic mixing time of ~10^3 y (23), δ^7Li of modern seawater is homogeneous.

In contrast, the lithium geochemical cycle during and immediately after the Marinoan snowball Earth would have been remarkably different from that of the modern ocean. This can be illustrated by considering an end-member scenario of a hard snowball Earth. During the Marinoan ice age, which lasted between 3.0 and 15.2 Myr (2), riverine Li flux into the ocean would have been attenuated relative to modern inputs due to a reduced hydrological cycle and limited chemical weathering on the continent. In contrast, silicate reverse weathering on the seafloor may have been faster due to generally higher dissolved silica concentrations (because biological sinks for the element were essentially absent in the Neoproterozoic), which would have accelerated clay mineral formation, leading to locally quantitative removal of lithium from diagenetic fluids and reducing the magnitude of Li isotopic fractionation (25). Thus, the attenuated riverine Li flux coupled with reduced isotopic fractionation would hypothetically lead to the preferential distillation of ^{7}Li from seawater during the glaciation, resulting in lower Li concentrations and δ^7Li values in ice-covered hypersaline seawater. Upon the termination of the Marinoan snowball Earth, thick sea ice would have melted first, followed by the melting of continental glaciers and the resumption of continental weathering. Since sea ice would contain little to no Li (28), it could dilute the hypersaline reservoir but would not change its δ^7Li composition, which would be recorded in the early stage of cap dolostone deposition (stage I). The melting of continental glaciers and the resumption of continental weathering would deliver ^{7}Li-rich fluids that floated above the aged and ^{7}Li-depleted hypersaline seawater. A ^{7}Li-rich riverine influx in the aftermath of the snowball Earth is conceivable considering the balance of (1) a strong hydrological cycle and warm temperatures and (2) superabundant silicate rock flour made available for chemical weathering by physical abrasion during the glaciation, leading to intermediate weathering intensities (i.e., weathering/denudation or W/D ratios) conducive to incongruent weathering (26). Thus, continental meltwater would have a δ^7Li value similar to or even higher than modern riverine influx (~23‰). The high δ^7Li values of postglacial riverine influx can also be recorded in the middle stage of cap dolostone deposition (stage II), particularly in nearshore surface waters where this flux may have exerted the strongest influence. Eventually, as the meltwater plume collapsed, both vertical and lateral isotopic gradients would be homogenized, and δ^7Li would return to lower values. Therefore, δ^7Li of the plumeworld ocean would be spatially and stratigraphically heterogeneous, and depending on the degree of synglacial distillation, the hypersaline seawater may have δ^7Li lower than that of the meltwater. Since Ediacaran cap dolostone was deposited in the plumeworld ocean, its δ^7Li values offer a powerful geochemical tool to assess the degree of synglacial distillation and the postglacial plumeworld ocean.

In this study, we analyzed lithium isotope compositions of the post-Marinoan cap dolostone of the Doushantuo Formation in South China (4). Our samples cover depositional facies from inner shelf to basinal environments that would be influenced by meltwater and hypersaline seawater to varying extents. Overall, the δ^7Li values are generally lower than those of Phanerozoic carbonates, and they also reveal an overall decreasing trend from platform to basinal facies. To interpret our data, a simple box model was constructed to show that δ^7Li data from the Doushantuo cap dolostone are consistent with an extremely limited riverine Li influx during the Marinoan glaciation and a plumeworld ocean in the aftermath.

Geological Setting and Sampling

The Ediacaran Doushantuo Formation in the Yangtze Block of South China (Fig. 1*A*) consists of carbonate, siltstone, black shale, and phosphorite that overlie glacial diamictites of the Marinoan-age Nantuo Formation and underlie the terminal Ediacaran Dengying Formation or its correlative Liuchapo Formation. The basal Doushantuo Formation is represented by a cap dolostone (Fig. 1*B* and *SI Appendix*, Figs. S1*A* and S2) that is a few meters in thickness, but is widely distributed across the Yangtze Platform from shelf to basinal environments (4). The cap dolostone is laterally persistent and traceable with generally consistent lithology

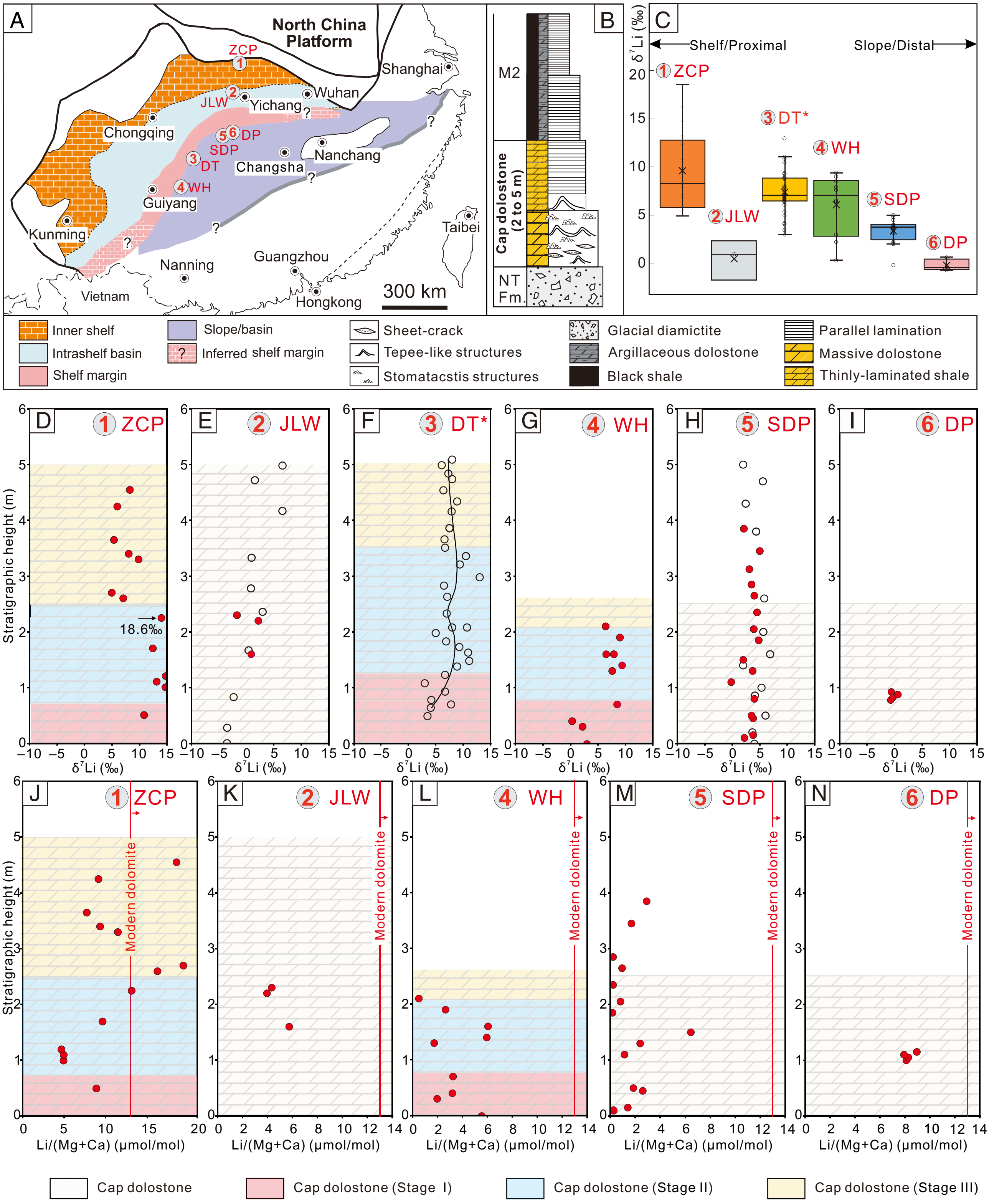

Fig. 1. Paleogeographic maps, stratigraphic columns, and δ⁷Li data from the post-Marinoan Doushantuo cap dolostone in South China. (*A*) Paleogeographic map showing depositional facies and approximate paleogeographical location of sample localities: Zhangcunping (ZCP), Jiulongwan (JLW), Daotuo (DT), Wuhe (WH), Siduping (SDP), and Daping (DP) sections, South China. (*A*) adapted from (33). (*B*) Generalized lithostratigraphic column of the Doushantuo cap dolostone, which is overlain by Member II (M2) of the Doushantuo Formation. See *SI Appendix*, Fig. S1 for detailed lithostratigraphic columns of all sampled sections. (*C*) Box-and-whisker plot of measured δ⁷Li data from six sections, arranged according to their paleogeographic location. The data of the DT section marked with an asterisk come from Taylor et al. (34). In each box and whisker plot, the box denotes interquartile range (IQR), horizontal line in the box represents the median, cross in the box represents the mean, whiskers represent 1.5 × IQR (or maximum/minimum values if they are within 1.5 × IQR). See (*D*–*I*) for chemostratigraphic plots of the same data. (*D*–*I*) Measured δ⁷Li data of Doushantuo cap dolostone at sampled localities. (*J*–*N*) Li/(Mg + Ca) ratios of Doushantuo cap dolostone at sampled localities. Previously published data from JLW and SDP by Yin et al. (35) and data from DT by Taylor et al. (34) are plotted as empty circles in (*E*, *F*, and *H*). Stages I–III, as recognized in previous work (13, 36–38) but applicable to the δ⁷Li profiles, represent cap dolostone deposition before the development of the plumeworld ocean, in a plumeworld ocean, and during the collapse of the plumeworld ocean (*SI Appendix*, Fig. S9).

and internal stratigraphy for at least 350 km in platform-to-basin transects (*SI Appendix*, Text 1). It consists of thick beds of thinly laminated dolostone accumulated below storm wave base (4). A distinctive suite of closely associated tepee-like structures, stromatactis-like cavities, layer-parallel sheet cracks, and cemented breccias occurs in the cap dolostone, particularly in the lower interval. While the top of the cap dolostone appears to grade into overlying strata in slope and basinal facies, it is marked by a locally developed karstic unconformity in inner shelf and shelf margin facies (*SI Appendix*, Figs. S1*A* and S2) (29, 30). Two indistinguishable zircon U–Pb ages from South China—a 634.6 ± 0.9 Ma age from the uppermost Nantuo Formation (31) and a 635.2 ± 0.6 Ma age from an ash bed immediately above the cap dolostone (32)—constrain the age of the cap dolostone to ~635 Ma.

Samples of the Doushantuo cap dolostone were collected from five sections at Zhangcunping (ZCP, N31°17′34″, E111°12′30″) and Jiulongwan (JLW, N30°48′54″, E111°03′20″) in Hubei Province, Daping (DP, N28°59′01″, E110°27′42″) and Siduping (SDP, N28°55′05″, E110°26′55″) in Hunan Province, and Wuhe (WH, N26°45′46″, E108°25′7″) in Guizhou Province (Fig. 1*A*). These sections, along with the previously published δ^7Li data from the Daotuo (DT) section in Guizhou Province (34), represent a transect from inner shelf to slope facies (Fig. 1*A*) (33). It is important to point out that the JLW section may represent deposition in a highly restricted intrashelf basin (39, 40), thus it may distort the general nearshore–offshore pattern if the transect is not represented broadly (35).

Results

Lithium isotope compositions of the 36 samples from the five sections were analyzed on a Q-ICP-MS at University of North Carolina at Chapel Hill (UNC), and 10 cap dolostone samples from the ZCP section were measured on a MC-ICP-MS at University of Maryland, College Park (UMD). The data, along with previously published δ^7Li data from the Jiulongwan and Siduping sections (35) and data from the Daotuo section (34), are presented in Fig. 1 *C–I* and *SI Appendix*, Fig. S1 *B–E* and Table S1. Twenty-six of these samples measured at UNC were also reanalyzed for δ^7Li on a MC-ICP-MS at UMD for interlaboratory comparison, and the results are presented in *SI Appendix*, Fig. S3 and Table S1. The two sets of data agreed excellently, although the UMD dataset has much better analytical uncertainties (approximately ±0.3‰, 2σ) than the UNC dataset (approximately ±1.9‰, 2σ). As a conservative treatment of analytical errors for the 26 duplicate analyses, we choose to use the UNC dataset for discussion, except for the ZCP section with a more complete UMD dataset. Consistent with the previously published data (34), the 46 new measurements show that the δ^7Li values range from –1.7 to 18.6‰ with an average of 5.4‰ (n = 46, SD = 4.5‰), which are significantly lower than those of previously published Precambrian (average = 7.7‰, n = 217, SD = 5.7‰; *P*-value ≈ 5.0×10^{-4}, one-tailed *t* test), Paleozoic (average = 10.1‰, n = 263, SD = 4.3‰, *P*-value ≈ 3.7×10^{-13}, one-tailed *t* test), and Cenozoic-Mesozoic carbonates (average = 23.1‰, n = 45, SD = 3.8‰, *P*-value ≈ 1.0×10^{-34}, one-tailed *t*-test) (25).

Although our sample preparation procedures were carefully designed to minimize clay mineral contamination during leaching experiments (41) (*SI Appendix*, Text 2), we attempted to assess and correct the measured δ^7Li values for potential clay mineral contamination using Al/(Mg + Ca) ratios (*SI Appendix*, Text 3 to 5 and Tables S2–S4). As clay minerals typically have lower δ^7Li values than carbonates (42), the corrected carbonate δ^7 Li values are expected to be higher than the measured values. The corrected δ^7Li values (*SI Appendix*, Fig. S1 *B–E*) have an average of 8.4‰ (n = 46, SD = 6.4‰) and range from –1.9 to 23.9‰, slightly higher than the measured δ^7Li values, but the spatial and stratigraphic trends remain unchanged, which is shown in *SI Appendix*, Table S1 and Fig. S1 *B–E*.

Both measured and corrected δ^7Li data show a decreasing trend from inner shelf (the ZCP section, $\text{average}_{\text{(measured)}}$ = 10.4‰, $\text{average}_{\text{(corrected)}}$ = 14.1‰, n = 13, Fig. 1*D* and *SI Appendix*, Fig. S1*B*) to slope facies in Guizhou (the WH section, $\text{average}_{\text{(measured)}}$ = 6.1‰, $\text{average}_{\text{(corrected)}}$ = 11.9‰, n = 10, Fig. 1*G* and *SI Appendix*, Fig. S1*D*) and Hunan (the SDP section, $\text{average}_{\text{(measured)}}$ = 3.4‰, $\text{average}_{\text{(corrected)}}$ = 4.8‰, n = 16, Fig. 1*H* and *SI Appendix*, Fig. S1*E*; the DP section, $\text{average}_{\text{(measured)}}$ = –0.3‰, $\text{average}_{\text{(corrected)}}$ = 1.0‰, n = 4, Fig. 1*I* and *SI Appendix*, Fig. S1*E*; combined $\text{average}_{\text{(measured)}}$ = 2.6‰, $\text{average}_{\text{(corrected)}}$ = 4.0‰). The intrashelf JLW section ($\text{average}_{\text{(measured)}}$ = 0.5‰, $\text{average}_{\text{(corrected)}}$ = 1.6‰, n = 3; Fig. 1*E* and *SI Appendix*, Fig. S1*C*) represents an anomaly to this trend. The overall difference in δ^7Li between the inner shelf and lower slope facies reaches $10.7‰_{\text{(measured)}}$ or $13.1‰_{\text{(corrected)}}$ (Fig. 1 *C–I* and *SI Appendix*, Fig. S1 *B–E*).

There are also stratigraphic variations at the ZCP and WH sections. At ZCP, δ^7Li starts at 10.8‰ (corrected value = 12.9‰, n =1; stage I in Fig. 1*D* and *SI Appendix*, Fig. S1*B*), then increases to an average of 15.0‰ (corrected value = 21.4‰, n = 5; stage II), and finally decreases to an average of 7.0‰ (corrected value = 9.1‰, n = 7; stage III) in the upper cap dolostone. At WH, δ^7Li starts with relatively low values at an average of 1.8‰ (corrected value = 5.5‰, n = 3; stage I in Fig. 1*G* and *SI Appendix*, Fig. S1*D*) and then stabilizes at higher values at an average of 7.9‰ (corrected value = 14.7‰, n = 7; stage II), consistent with the δ^7Li stratigraphic trends of the Doushantuo cap dolostone at the DT section (34). These stages are not recognized at the JLW, SDP, and DP sections, possibly because of insufficient stratigraphic coverage, restricted intrashelf basin at JLW (39, 40), or slight diachroneity of the cap dolostone at different sections on the time scale of 10^3 y (43). Similar to δ^7Li values, Li/(Mg + Ca) ratios also show a stratigraphic pattern with an increase followed by a decreasing trend, best expressed at ZCP, WH, and SDP (Fig. 1 *J–N*).

Discussion

Diagenesis and Clay Mineral Contamination. In order to interpret the variable Li isotopic compositions of the Doushantuo cap dolostone across the South China basin in the context of the plumeworld hypothesis, we should have confidence that the δ^7Li values in different localities and stratigraphic positions within each unit reflect evolving depositional conditions. Like all geological samples, the Doushantuo cap dolostone undoubtedly experienced diagenesis. The question most relevant to this study is whether diagenetic alteration significantly modified the spatial and stratigraphic patterns of carbonate δ^7Li, and whether it can account for the observed geochemical patterns.

We used petrographic observations and geochemical data to assess the potential for diagenetic alteration of δ^7Li (44). Detailed hand sample and thin section observations (*SI Appendix*, Fig. S4) and diagenetic screening by geochemical proxies—including δ^{18}O, Rb/Sr, Mn/Sr, Mn/(Mg + Ca), and Sr/(Mg + Ca) (*SI Appendix*, Fig. S5)—suggest minimal diagenetic alteration of δ^7Li values, with the possible exception of the WH section. Importantly, the spatial and stratigraphic patterns of the δ^7Li values cannot be explained by diagenetic alteration alone (*SI Appendix*, Text 3).

To aid in the assessment of clay mineral contamination during sample leaching processes, the leachate for δ^7Li measurement was also analyzed for elemental concentrations. Because clay and carbonate minerals have significantly different Al and Rb concentrations, these elements were chosen as proxies for clay contamination. The Rb/(Mg + Ca) ratios of Doushantuo cap dolostone samples (n = 46) range from 0.06×10^{-6} to 2.37×10^{-6} ppm/ppm (*SI Appendix*, Fig. S5*A*), all below the proposed threshold value of 3.0×10^{-5} ppm/ppm (25), suggesting minimal clay mineral contamination. In contrast, Al/(Mg + Ca) ratios of Doushantuo cap dolostone samples range from 0.19×10^{-3} to 9.31×10^{-3} ppm/ppm (*SI Appendix*, Fig. S5*B*), and many are above the 0.54×10^{-3} ppm/ppm threshold chosen to screen for clay contamination (25). Nonetheless, no correlation is observed between either measured or corrected δ^7Li values and element ratios of Rb/(Mg + Ca), Al/(Mg + Ca), and Li/(Mg + Ca) (*SI Appendix*, Fig. S5 *A–C*), indicating that clay mineral contamination is unlikely to be a major driver of the observed δ^7Li variations. To further assess clay mineral contamination in samples with elevated Al/(Mg + Ca) ratios, Monte Carlo modeling was conducted to quantify the probability of likely clay content in our samples (*SI Appendix*, Text 4). The model suggests that the maximum probability corresponds to a clay mineral content ≤ 0.5 wt.% (*SI Appendix*, Figs. S6 and S7).

As stated in the *Results* section, an effort was made to correct the measured δ^7Li for potential clay mineral contamination because even 0.5 wt.% clay mineral contamination could have a notable impact on δ^7Li owing to the higher Li content of clay compared to carbonate minerals. Taking into consideration that clay minerals typically have lower δ^7Li values than carbonates (42), we use a binary mixing model to show that the corrected carbonate δ^7Li values could be 1 to 6‰ higher than the measured values (*SI Appendix*, Text 5 and Table S4). However, the corrected data do not change the temporal and nearshore–offshore patterns of δ^7Li.

The Depositional Setting. Sedimentological evidence indicates that the Doushantuo cap dolostone was deposited in a marine environment below storm wave base, in contrast to Paleozoic and modern dolostones, which are typically found in evaporitic or lagoonal conditions. However, if kinetic barriers (*SI Appendix*, Text 3) were overcome in the postglacial plumeworld (due to increased temperature, freshening of seawater, reduction or dilution of sulfate, and wholesale precipitation of calcium carbonate), cap dolostone could have formed in relatively deep waters across the basin. The lower Doushantuo cap dolostone is characterized by widespread and persistent facies containing ubiquitous tepee- and stromatactis-like cavities that have been interpreted as related to methane cold seeps (4). Similar cavities and cements have been observed in cap dolostones from Australia (45), Namibia (7, 46), eastern California (47), and Norway (48). If the cold seep environmental interpretation is correct (8), methanogenic mats must have carpeted the seafloor across the basin, and sulfate reduction would likely have been the dominant recycling metabolism creating alkalinity and primary dolomite (49). We envision that sea level could have risen rapidly during the deglaciation, so this phenomenon could have been broadly isochronous, or it could have happened more slowly, and the cap dolostones were slightly diachronous (43, 50). In the latter model, as sea level progressively rose during the deglaciation, the locus of cap dolostone accumulation would have moved up the continental slope and then onto the continental platform; however, as long as the timescale of cap dolostone diachroneity (43) did not exceed that of plumeworld persistence estimated to be 10^3 to 10^4 y (15, 16) or the duration of the cap dolostone (31, 51), the nearshore–offshore gradient should still be recorded in cap dolostone sections deposited along the gradient. In either case, distal settings would have accumulated Li from the evolved seawater, while more proximal ones would have felt the effects of Li in the continental meltwater plume. This is driven by both the vertical stratification and lateral gradient as predicted by the plumeworld hypothesis.

Low δ^7Li Values, Synglacial Distillation, and Reverse Weathering. Broadly consistent with a previous compilation of Precambrian carbonate δ^7Li values (25), the average δ^7Li value of Doushantuo cap dolostone samples (8.4‰) is markedly lower than that of modern carbonates (>20‰) (44, 52). This indicates that the δ^7Li values of Neoproterozoic seawater were substantially lower than that of modern oceans (31‰). The lower δ^7Li values of Precambrian seawater have been interpreted as the result of muted isotopic fractionation in association with clay authigenesis on the seafloor (25). Because of the scarcity of Si-biomineralizing organisms in Precambrian oceans, the concentration of dissolved silica was high, leading to high rates of reverse weathering, low isotopic fractionation in association with clay authigenesis, reduced removal of the light Li isotope from Precambrian oceans, and consequently low δ^7Li values of Precambrian seawater and carbonate proxies (25, 53). This may also be true during the snowball Earth when continental weathering was limited, because silicon and iron needed for reserve weathering can be supplied from hydrothermal input, as evidenced by the deposition of banded iron formations following the Sturtian snowball Earth (2). As an end-member scenario, it is possible that reverse weathering rate was so high that Li^+ with high affinity for clay minerals may have been quantitatively removed from porewater, resulting in near-zero isotopic fractionation between porewater and clays (54). Furthermore, laboratory experiments have shown that the formation of particular types of clays in seawater may have limited Li isotopic fractionation; for example, synthetic saponite and stevensite have $\Delta_{\text{Seawater–Sediment}}$ as low as 4.4‰ (55), and the interlayer complexation in smectite barely causes any Li isotopic fractionation (56). We note that the average δ^7Li value of 2.6‰ (corrected value= 4.0‰) from the lower-slope Doushantuo cap dolostone at the SDP and DP sections is even lower than the average δ^7Li value (7.7‰) of Precambrian carbonates (25), suggesting that additional factors may have affected the seawater $\delta^7\text{Li}_{\text{SW}}$ values during the Marinoan snowball Earth.

Inference of post-Marinoan $\delta^7\text{Li}_{\text{SW}}$ from the $\delta^7\text{Li}_{\text{dolomite}}$ values of the Doushantuo cap dolostone is associated with several sources of uncertainty. These include the poorly constrained isotope fractionation during dolomite precipitation ($\Delta_{\text{dolomite–SW}}$), spatial and chemostratigraphic variations in $\delta^7\text{Li}_{\text{dolomite}}$ of the Doushantuo cap dolostone, potential clay mineral corrections as discussed above, and analytical uncertainty. We have demonstrated that clay contamination and analytical uncertainty are relatively minor, and they do not account for the low values and observed spatial pattern of δ^7Li values. Therefore, the following discussion will focus on the uncertainty in isotope fractionations and the spatial and chemostratigraphic variations.

Some studies have suggested that dolomite formed under fluid-buffered diagenetic conditions in the Great Bahama Bank and South China Sea has $\delta^7\text{Li}_{\text{dolomite}}$ values similar to that of modern seawater (44, 52, 57), indicating a $\Delta_{\text{dolomite–SW}}$ value of ~0‰. If so, $\delta^7\text{Li}_{\text{dolomite}}$ values of the Doushantuo cap dolostone would mean a very low $\delta^7\text{Li}_{\text{SW}}$ composition; for example, average $\delta^7\text{Li}_{\text{dolomite}}$ of the lower slope facies (the SDP and DP sections where seawater influence would have been the strongest) would mean a $\delta^7\text{Li}_{\text{SW}}$ value of ~3 to 4.0‰. Other studies have shown that stronger isotopic fractionation associated with calcite/aragonite precipitation ($\Delta_{\text{calcite/aragonite–SW}}$) is averaged around −10‰ (58–60). If this fractionation applies to cap dolomite precipitation, then the average $\delta^7\text{Li}_{\text{dolomite}}$ value of the lower slope facies would mean a $\delta^7\text{Li}_{\text{SW}}$ value of 13 to 14‰.

We used a mass balance model (61) to test whether synglacial distillation in an ice-covered ocean during the Marinoan glaciation could drive δ^7Li_{SW} from a modern seawater value of 31 to ~13‰ as needed to explain the lower slope $\delta^7Li_{dolomite}$ data (Fig. 2 and *SI Appendix*, Text 6 and Fig. S8). For a conservative assessment, we set the pre-Marinoan δ^7Li_{SW} to the modern seawater value of 31‰ and the model tracks δ^7Li_{SW} throughout the glaciation to see whether post-Marinoan δ^7 Li_{SW} can reach 13‰. The post-Marinoan target δ^7Li_{SW} of 13‰ is informed by the average $\delta^7Li_{dolomite}$ value of the lower slope facies data (3 to 4‰) and an average $\Delta_{dolomite–SW}$ of −10‰, which is further explained in *SI Appendix* (*SI Appendix*, Text 6). We emphasize that the model is for illustrative purposes and not meant to reproduce the exact δ^7Li_{SW} values because of the large uncertainty associated with the inversion of δ^7Li_{SW} from $\delta^7Li_{dolomite}$.

In this model, the seawater lithium reservoir (M) depends on the influxes from riverine input (F_{riv}) and high-temperature alteration at the mid-ocean ridges (F_{HT}), as well as outfluxes through authigenic clay mineral formation (F_a) and low-temperature alteration (F_{LT}). The isotopic composition of seawater (δ^7Li_{SW}) depends on the size of the lithium reservoir, influxes, outfluxes, and their isotopic compositions (δ^7Li_{riv} and δ^7Li_{HT}) or fractionation factors ($\Delta^7Li_a = \delta^7Li_a - \delta^7Li_{SW}$ and $\Delta^7Li_{LT} = \delta^7Li_{LT} - \delta^7Li_{SW}$). We set the model time to 10 Myr in light of the estimated duration of the Marinoan glaciation of <15 Myr and most likely ~12 Myr (2, 62). The high-temperature input (F_{HT} and δ^7Li_{HT}) was set the same as modern values since geophysical models estimate hydrothermal heat flux to be near-modern and to have stayed constant during our studied time interval (63, 64). A series of sensitivity tests were performed to explore a wide range of possible values for F_{riv} (0%, 10%, and 20% of modern values; Fig. 2 and *SI Appendix*, Fig. S8*A*), Δ^7Li_a (−20 to 0‰; Fig. 2 and *SI Appendix*, Fig. S8*C*), Δ^7Li_{LT} (−18‰, −10‰, and −8‰; Fig. 2 and *SI Appendix*, Fig. S8*C*), δ^7Li_{riv} (1‰ to the modern value of 23‰; *SI Appendix*, Fig. S8*A*), preglacial δ^7Li_{SW} (10‰ to the modern value of 31‰; *SI Appendix*, Fig. S8*B*), and δ^7Li_{HT} (*SI Appendix*, Fig. S8*C*).

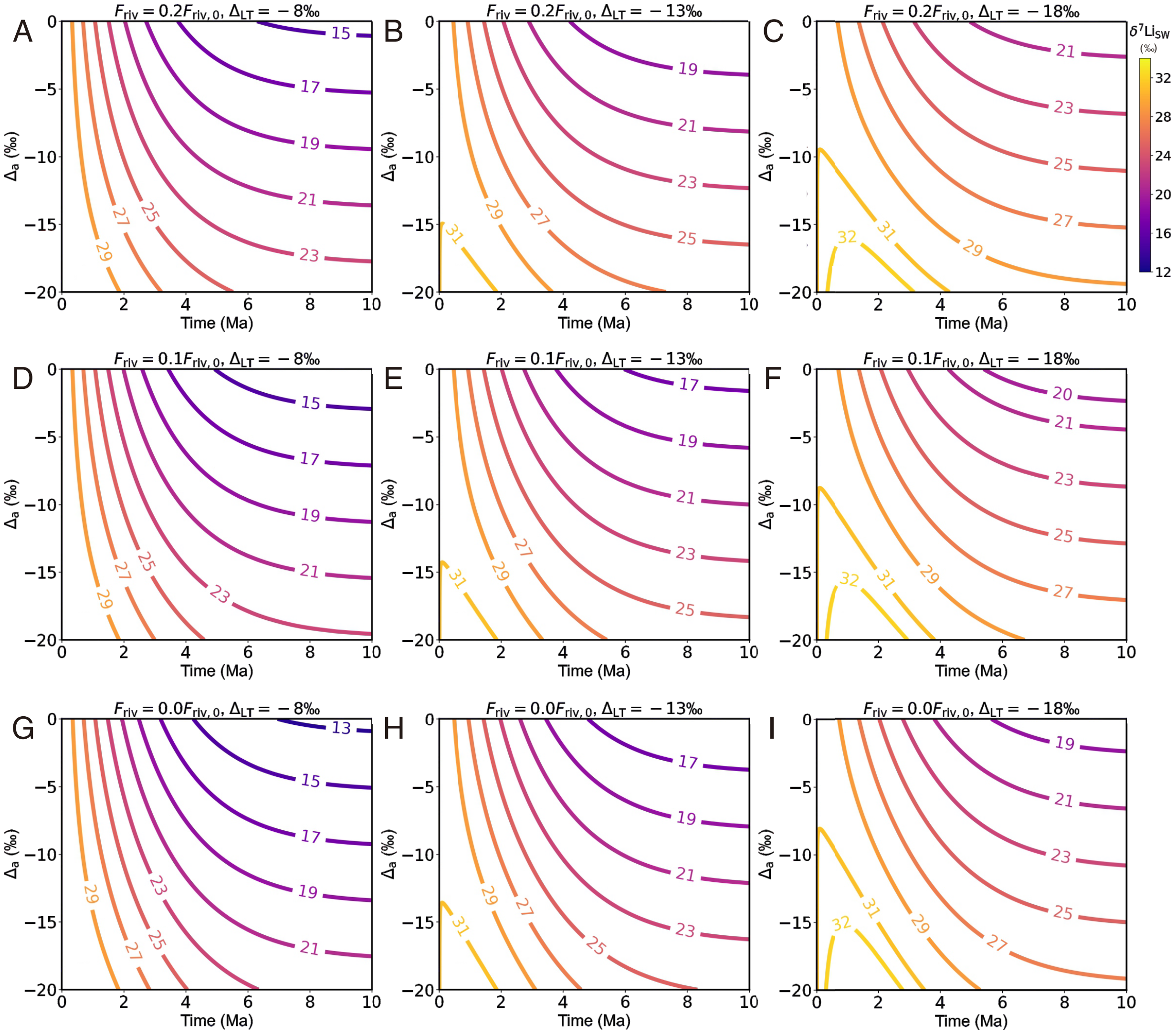

Fig. 2. Model results of seawater Li isotope evolution during snowball Earth. Contours and color scale represent seawater Li isotope values (δ^7Li_{SW}) as a function of three variables: riverine flux (F_{riv}), isotopic fractionation associated with marine authigenic clay mineral formation ($\Delta^7\mathbf{Li}_a = \boldsymbol{\delta}^7Li_a - \boldsymbol{\delta}^7Li_{SW}$), and isotopic fractionation associated with low-*T* seafloor alternation ($\Delta^7Li_{LT} = \boldsymbol{\delta}^7Li_{LT} - \boldsymbol{\delta}^7Li_{SW}$). The riverine flux F_{riv} is set at 20% (*Top row*; *A*–*C*), 10% (*Middle row*; *D*–*F*), and 0% (*Bottom row*; *G*–*I*) of modern flux. Along each row, Δ^7Li_{LT} is set at −18‰ (*Right column*; *C*, *F*, and *I*), −13‰ (*Middle column*; *B*, *E*, and *H*), and −8‰ (*Left column*; *A*, *D*, and *G*). The y-axis Δ^7Li_a varies from −20 to 0‰. All other parameters are held constant and are equal to their modern values (*SI Appendix*, Table S5). Initial values of δ^7Li_{SW} and *M* in the model are both the same as their modern ocean values. Sweep in this three-parameter space highlights a scenario (panel *G*) where δ^7Li_{SW} can evolve to be as low as 13‰ on a timescale of ~7 to 8 Myr when riverine flux is vanishingly small (F_{riv} = 0) and Li isotope fractionation associated with reverse weathering is muted ($\Delta^7Li_a \approx 0$), consistent with reduced chemical weathering on continent and enhanced reverse weathering on seafloor during the snowball Earth.

Additional parameter details for the model are provided in the *SI Appendix*, Table S5.

The model results show that within the parameter space explored, $\delta^7\text{Li}_{SW}$ can evolve from a modern seawater value of 31 to <13‰ on a timescale of ~7 to 8 Myr when the riverine flux is low ($F_{riv} \approx 0\%$ of modern value) and the isotopic fractionation associated with authigenic clay mineral formation and low-temperature alteration is limited ($\Delta^7\text{Li}_a \approx 0‰$; $\Delta^7\text{Li}_{LT} \approx -8‰$) (Fig. 2*G*). A low riverine flux would be expected during a snowball Earth, particularly toward the peak of glaciation (1, 6). Additionally, elevated reverse weathering, driven by the high concentrations of dissolved silica in Precambrian oceans prior to the ecological rise of Si-biomineralizing organisms (53), may have effectively limited Li isotopic fractionation during rapid formation of authigenic clay minerals (25), favoring the evolution toward lower $\delta^7\text{Li}_{SW}$ values. A low riverine $\delta^7\text{Li}_{riv}$ composition (<13‰) can also drive $\delta^7\text{Li}_{SW}$ to lower values (*SI Appendix*, Fig. S8*A*), although it is uncertain whether $\delta^7\text{Li}_{riv}$ would have been lower during the Marinoan snowball Earth relative to before and after the ice age. On the one hand, congruent continental weathering of silicates would be expected during the glaciation because of low chemical weathering rates. On the other hand, a recent study suggests that silicate weathering on continents during glacials tends to be incongruent compared to interglacials, as inferred from $\delta^7\text{Li}$ values recorded in speleothems (65). Nonetheless, as long as isotopic fractionation associated with the outfluxes is limited ($\Delta^7\text{Li}_a \approx 0‰$; $\Delta^7\text{Li}_{LT} \approx -8‰$), a $\delta^7\text{Li}_{SW}$ value of <13‰ is possible through synglacial distillation either when F_{riv} approaches to 0% of modern value (Fig. 2) or when $\delta^7\text{Li}_{riv}$ is lower than 13‰ (*SI Appendix*, Fig. S8*A*). It does not necessarily require both low F_{riv} and low $\delta^7\text{Li}_{riv}$. This conclusion is insensitive to the choice of preglacial $\delta^7\text{Li}_{SW}$ values (*SI Appendix*, Fig. S8*B*). Given the uncertainty with regard to congruent vs. incongruent continental weathering of silicates during glaciations, we favor a low F_{riv} as a key driver, considering that chemical weathering flux was likely low during the Marinoan glaciation. Thus, it is plausible that evolved seawater at the end of the Marinoan snowball Earth could have a $\delta^7\text{Li}_{SW}$ value of ~13‰ (Fig. 3*B*), much lower than that of the modern seawater (31‰) and even lower than that of the modern riverine input (23‰). If so, upon the termination of the snowball Earth when riverine input resumes, the Li isotopic gradient between seawater and riverine input (or freshwater plume) would be reversed (Fig. 3*C*) relative to the modern ocean (Fig. 3*A*).

Li Isotope Evidence for a Post-Marinoan Plumeworld Ocean. A reversed $\delta^7\text{Li}$ gradient between evolved seawater and riverine input is consistent with the observed spatial trend in $\delta^7\text{Li}$ of the Doushantuo cap dolostone, supporting plumeworld hypothesis. This hypothesis predicts that the meltwater plume and, hence, the vertical stratification and $\delta^7\text{Li}$ gradient would be sustained for ~10^3 to 10^4 y (11, 15, 16). A nearshore–offshore gradient may be dynamically maintained as well, as long as there is a continuous supply of continental glacier meltwater. Insofar as the duration of the cap dolostone is similar to or greater than the longevity of the meltwater plume and its diachroneity is less (43), the spatial and temporal dynamics of the plumeworld ocean should be recorded in cap dolostone deposits. Indeed, the overall spatial gradient in $\delta^7\text{Li}$ of the Doushantuo cap dolostone, from 10.4‰ in inner shelf facies to 6.1‰ in upper slope facies and to 2.6‰ in lower slope facies, is broadly consistent with a plumeworld ocean and can be explained by variable degree of isotopic mixing between riverine input from glacial meltwater and evolved hypersaline seawater (11). In other words, cap dolostones deposited in the inner-shelf environment would have been more strongly influenced by the meltwater plume and have higher $\delta^7\text{Li}$ values than those in slope settings where aged hypersaline seawater asserted a greater influence.

The Jiulongwan (JLW) data stand as an outlier from the overall spatial trend of decreasing $\delta^7\text{Li}$ values from shelf to slope

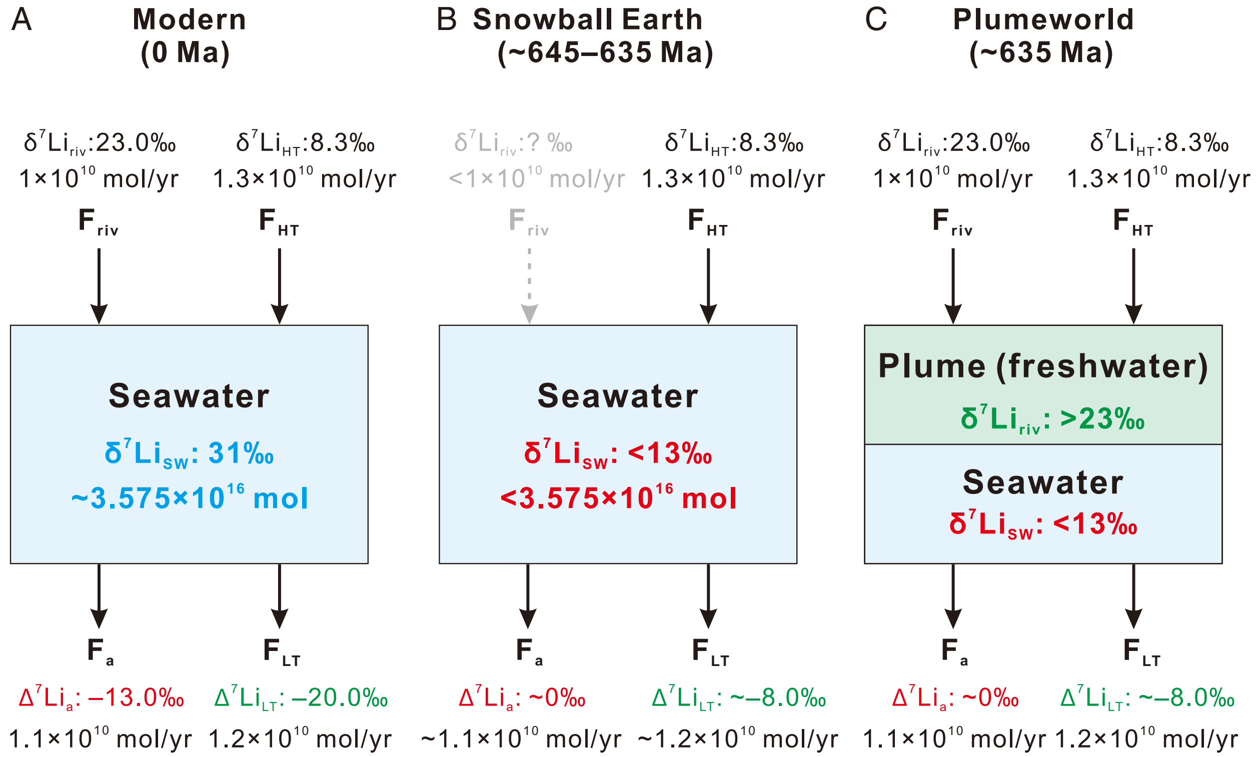

Fig. 3. Schematic lithium cycle in the modern ocean (*A*, modified after ref. 66), in a snowball Earth ocean (*B*, based on Figs. 2*G* and 3), and in a plumeworld ocean (*C*). Note that in the snowball Earth ocean (*B*), the riverine Li flux (F_{riv}) has been marked in gray, denoting a diminished riverine input of Li. A $\Delta^7\text{Li}_a$ value of ~0‰ is chosen to illustrate conditions during the snowball Earth as informed by the most favorable modeling scenario (Fig. 2*G*, *Upper Right*).

environments. It is possible that the cap dolostone from Jiulongwan accumulated in a restricted intrashelf lagoon (39, 40). Stratigraphic evidence for such a scenario comes from the distribution of karst atop the cap dolostone: the inner-shelf (ZCP) and shelf margin (e.g., Weng'an section) cap dolostones are strongly karstified with clear topographic reliefs (30), but there is little topographic relief at the inferred exposure surface atop the cap dolostone at the Jiulongwan section, indicating a rimmed platform with topographic highs at both inner shelf and shelf margin, but topographic low in the intrashelf basin. While some consider that the intrashelf lagoon developed *after* the deposition of the Doushantuo cap dolostone (33), we argue that it was initiated *during* the Marinoan ice age by glacial scouring (29). Thus, the intrashelf lagoon may depart from the general nearshore–offshore gradient of δ^7Li.

We note that a previous study of the Doushantuo cap dolostone reported a spatial trend of *increasing* δ^7Li values from shelf to slope facies using data from two sections (35) rather than the *decreasing* trend we demonstrate here from five. However, that study was based on the Jiulongwan (JLW) and Siduping (SDP) sections, so that the anomalous data from the aberrant JLW section drove the spatial pattern they documented. In contrast, our more complete coverage of the nearshore–offshore transect shows an overall pattern of decreasing δ^7Li values from the shallow shelf to the slope, consistent with synglacial distillation of saline seawater, as well as a postglacial plumeworld.

The plumeworld model may also help to explain the δ^7Li chemostratigraphic trend observed in the Doushantuo cap dolostone (Fig. 4). The more complete chemostratigraphic profiles in the upper slope environment show that the basal cap dolostone (stage I) has the lowest δ^7Li values and lowest Li/(Mg + Ca) ratios (Fig. 1 *G* and *L* and *SI Appendix*, Fig. S1*D*). These low values are consistent with the predicted low δ^7Li values and Li concentrations in evolved hypersaline seawater (Fig. 4*B*). We hypothesize that stage I cap dolostone was deposited during early deglaciation but prior to the development of the plumeworld ocean, and was thus strongly influenced by hypersaline seawater (Fig. 4*C*). During this stage, the melting of sea ice may have diluted the Li concentrations of seawater, but it would not have influenced the $\delta^7\text{Li}_{\text{SW}}$ value because sea ice contains little Li.

In stage II, a meltwater plume formed, nearshore–offshore and vertical δ^7Li gradients developed, and stage II cap dolostone at different localities was variously influenced by the mixing of meltwater plume and hypersaline seawater (Fig. 4*D*). Because of intense postglacial weathering of large amounts of silicate rock flour generated during the glaciation (5), terrestrial meltwater was rich in alkalinity and characterized by high δ^7Li values (due to incongruent continental weathering of silicates). Thus, in addition to the vertical and lateral gradients discussed above, there is also an overall increase in both δ^7Li and Li/(Mg + Ca) from stage I to stage II (Fig. 1 *G* and *L* and *SI Appendix*, Fig. S1*D*), reflecting the arrival of a meltwater plume from the terrestrial realm. We note that this

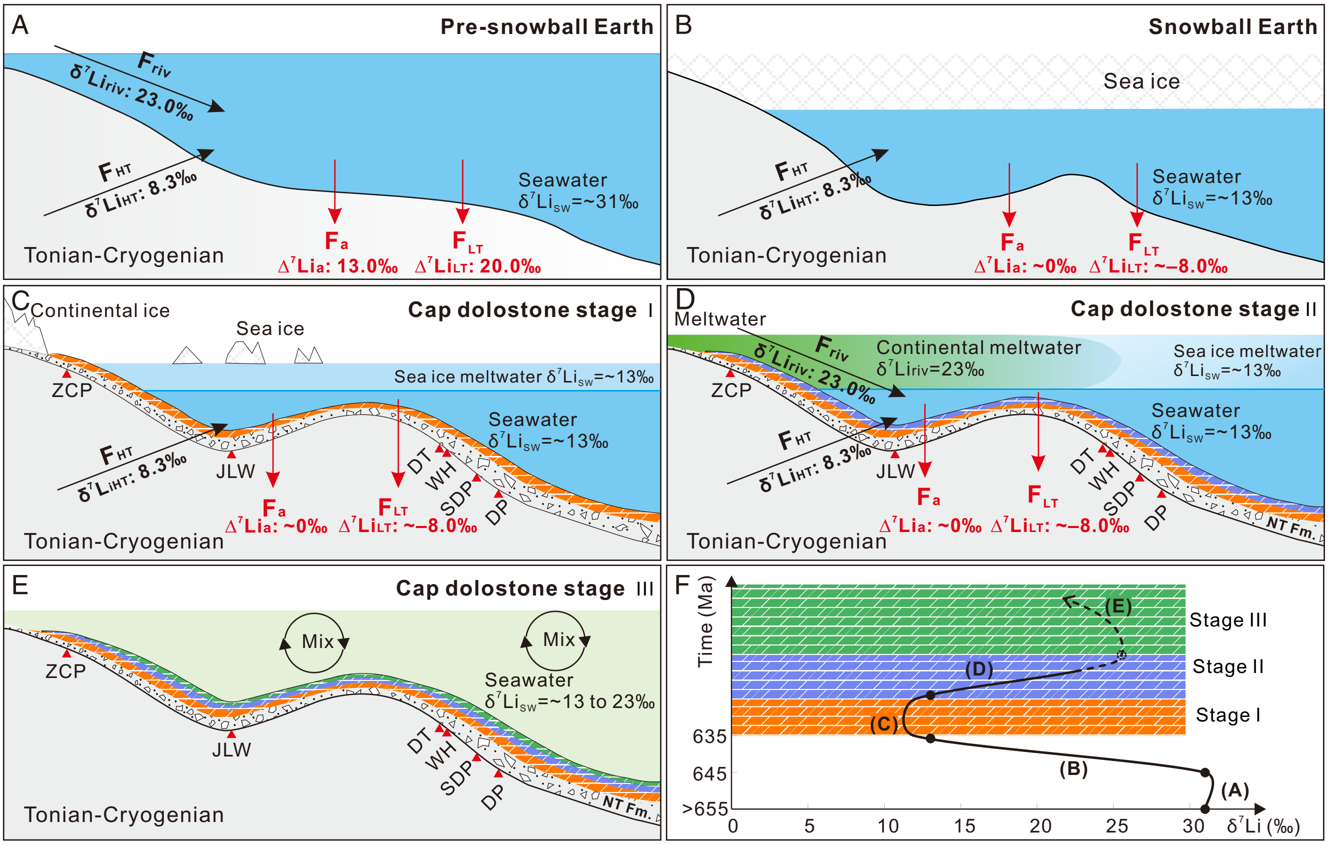

Fig. 4. Schematic diagrams showing lithium cycles before, during, and after the Marinoan snowball Earth event [modified from (13)]. (*A*) Pre-snowball ocean with lithium reservoir size and fluxes similar to those in modern ocean. (*B*) Syn-glacial ocean, showing the end-member scenario of a hard snowball Earth. (*C*) The first stage of cap dolostone deposition during the melting of sea ice. The geochemistry of stage I cap dolostone is strongly influenced by the low $\delta^7\text{Li}_{\text{SW}}$ of hypersaline seawater. (*D*) The second stage of cap dolostone deposition, showing freshwater plume from terrestrial meltwater that imparts higher δ^7Li values to the cap dolostone. (*E*) The third stage of cap dolostone precipitation, showing the collapse of the plumeworld, mixing of meltwater and seawater, and return of cap dolostone δ^7Li to lower values. (*F*) Idealized cartoon showing the evolution of seawater $\delta^7\text{Li}_{\text{SW}}$ values before, during, and after the snowball event in places where the meltwater plume can reach. Labels (*A*–*E*) on the curve correspond to panel (*A*–*E*), and the three stages of cap dolostone deposition correspond to those marked in Fig. 1 *D*–*G*.

stratigraphic trend is not observed at all sections, possibly because of poor stratigraphic coverage (e.g., JLW and DP) or limited extent of the meltwater plume (e.g., not reaching lower slope sections at SDP and DP). The average stage II δ^7Li of 15.0‰ (measured) and 21.4‰ (corrected) in the inner shelf section at ZCP may be taken as an approximation of the meltwater plume δ^7Li composition (Fig. 1*D* and *SI Appendix*, Fig. S1*B*), which would be 15.0 to 25.0‰ and 21.4 to 31.4‰ depending on $\Delta_{\text{dolomite–fluid}}$, indicating incongruent continental weathering of silicates in the aftermath of the Marinoan glaciation.

Finally, the stage III cap dolostone may have witnessed the collapse of the plumeworld and the mixing of meltwater and seawater (Fig. 4*E*) or a shift to more congruent silicate weathering on continents, as evidenced by the return of δ^7Li to lower values (Fig. 1*D* and *SI Appendix*, Fig. S1*B*). We note that the stratigraphic trends are not as robust as the spatial pattern, partly because of variable stratigraphic coverage, and also because the exact shape of the chemostratigraphic profile depends on the paleobathymetric location (hence the mixing ratio of the meltwater and seawater) and is further complicated by the small-scale diachroneity of cap dolostone (43). However, the chemostratigraphic trend is bolstered by other geochemical proxies. For example, the three stages of cap dolostone deposition can also be recognized on the basis of δ^{44}Ca, ^{87}Sr/^{86}Sr, ^{88}Sr/^{86}Sr, and δ^{26}Mg (13, 36–38) (*SI Appendix*, Fig. S9). Stage II cap dolostone is characterized by geochemical signatures of a terrestrial meltwater plume, with lower δ^{44}Ca, higher ^{87}Sr/^{86}Sr, and lower δ^{26}Mg values than stage I and stage III cap dolostone. Together, multiple lines of geochemical evidence offer support to the plumeworld hypothesis and point to a physically and chemically dynamic ocean system at the end of the Marinoan snowball Earth.

Summary. Lithium isotope data from the Ediacaran Doushantuo cap dolostone in South China are consistent with reduced continental weathering on the continent and enhanced reverse silicate weathering on the seafloor during the Marinoan snowball Earth, as well as a plumeworld ocean in its aftermath. The δ^7Li values are lower than those of Phanerozoic carbonates, and they show a decreasing trend from inner shelf to slope facies. We hypothesize that the spatial trend reflects differential mixing between meltwater with a relatively high $\delta^7\text{Li}_{\text{riv}}$ value and evolved hypersaline seawater with a low $\delta^7\text{Li}_{\text{SW}}$ value, irrespective of whether the caps were isochronous or diachronous on the timescale of 10^3 to 10^4 y. The cap dolostone δ^7Li gradient from proximal and distal facies is thus consistent with a postglacial plumeworld ocean, where a persistent, terrestrially derived meltwater plume occurred nearshore and on top of evolved hypersaline seawater. The Doushantuo cap dolostone also exhibits a recognizable stratigraphic trend, beginning with low δ^7Li and Li/(Mg + Ca) values followed by an increasing and then a decreasing trend. Although this chemostratigraphic trend remains to be confirmed, it is also consistent with the development of a postglacial meltwater plume, reflecting the influence of evolved seawater at the beginning of cap dolostone deposition, followed by increasing impact of terrestrial meltwater and then mixing of meltwater and seawater. Additionally, the inferred δ^7Li composition of the evolved seawater (~13‰) requires isotopic distillation of the ocean during the Marinoan snowball Earth, with little riverine influx from continental weathering and muted isotopic fractionation associated with enhanced reverse weathering of the seafloor in a silica-rich ocean. The lithium isotope data presented here may ultimately allow us to test the severity of the Marinoan glaciation, as well as extreme biogeochemical reorganization associated with its aftermath.

Methods

Lithium Isotopic Analyses and Elemental Analyses. Lithium isotope compositions of 36 samples were analyzed using quadrupole inductively coupled plasma mass spectrometry (Q-ICP-MS, Agilent™ 7,900) at the University of North Carolina, Chapel Hill (UNC). Lithium isotope ratios were measured using the standard-sample bracketing method (67). After lithium chromatographic purification (67, 68), samples and lithium standard IRMM-016 were diluted to 0.5 ng/g in 2% nitric acid to match matrix. Lithium was then introduced through a PFA nebulizer and analyzed under the hot plasma (1,550 W) condition. The integration time for ^{7}Li and ^{6}Li are 1 s and 12 s, respectively. Each analysis consisted of 1,000 integrations and was repeated 7 times, followed by a long washing time (180 s) to decrease memory effects. Li isotope compositions were expressed relative to the IRMM-016 Li standard, defined as $\delta^7\text{Li}(‰) = [(^7\text{Li}/^6\text{Li})_{\text{sample}}/(^7\text{Li}/^6\text{Li})_{\text{IRMM-016}}] - 1 \times 1{,}000$. The long-term external precision is 1.1‰ (67).

Ten samples from ZCP section (sample number ZCP-× ×) and 26 sample solutions of the 36 samples analyzed at UNC were measured for δ^7Li on a Thermo Scientific Neptune Plus MC-ICP-MS with an Apex-IR inlet system in Department of Geology at University of Maryland, College Park (UMD); the 26 duplicate analyses were conducted for interlaboratory comparison. Lithium isotopes were measured with a 50 μL/min PFA nebulizer at low resolution using X skimmer and Jet sampler cones. A typical ^{7}Li signal intensity was 2 to 3 V for 5 ppb Li solution. Samples and the international lithium standard LSVEC were diluted to 5 ppb in 2% nitric acid to match matrix, and δ^7Li values were analyzed using a standard-sample bracketing method relative to the LSVEC standard. Each sample was measured three separate times to report SD (2SD), and each individual measurement consisted of 40 cycles in one block with 4.194 s integration time for each cycle. Nitric acid (2%) was measured before each sample and standard for background subtraction. Accuracy and precision were also assessed from repeated measurements of a 5 ppb in-house standard (UMD-1), reporting δ^7Li 55.3‰ ± 0.4 (2SD, n = 22), in good agreement with the published values of δ^7Li 54.7 ± 1.0‰ (2SD, n = 31) (69).

Aliquots of the 36 samples analyzed for δ^7Li at UNC were measured for elemental concentrations on an Agilent Q-ICP-MS at UNC, using the ultra-high matrix introduction (UHMI) mode. Samples were calibrated against matrix-matched multielement standards before being analyzed under UHMI mode, in which helium gas was used to reduce potential isobaric interferences. Background intensities were monitored periodically by aspirating 2% v/v HNO_3 blank, and an internal standard solution containing Be, Ge, In, and Bi was used to correct for the instrumental drift. A limestone standard, NIST-1d, obtained from the National Institute of Standards and Technology (NIST), was measured routinely, yielding long-term accuracy of <10% for major elements (70).

Aliquots of the 10 samples analyzed for δ^7Li at UMD were measured for elemental concentrations on a Thermo Scientific® iCAP-Q ICP-MS at the Arizona State University, operated in both standard mode and kinetic energy dispersion (KED) mode using He in the collision cell. All elements, except for B and Li, were analyzed in KED mode to eliminate polyatomic interference species, and this was followed by standard measurement mode (i.e., no collision gas) for B and Li. A custom internal standard composed of 400 ppb Sc, and 200 ppb of Ge, In, and Bi was introduced with the sample at equal flow rates to the spray chamber to account for sample matrix variation and the high-frequency ionization physics inherent to plasma techniques. External calibration relies on in-house calibration solutions prepared gravimetrically from certified single-element standards, and the calibration is validated with several QA/QC solutions of known composition to ensure results match within usual accuracy and precision limits.

Data, Materials, and Software Availability. All geochemical data generated here are included in *SI Appendix*, Table S1. A description of the Li mass-balance model and quantifying clay contamination through Monte Carlo sampling are available in *SI Appendix*. Additional code (in Python) has been posted on Zenodo (61). All other data are included in the manuscript and/or *SI Appendix*.

ACKNOWLEDGMENTS. We thank Richard D. Ash, Sarah C Penniston-Dorland, Jan Hellmann, and Geoffrey J. Gilleaudeau for help with lithium isotope analysis. We thank Shiji Zheng and Haibo Qin for their help with sample collection. This research was supported by the NSF (EAR-2021207 to S.X. and EAR-2020593 to A.J.K.), the Patricia Caldwell Faculty Fellowship at Virginia Tech, the University of North Carolina at Chapel Hill, and the National Natural Science Foundation of China (U1812402). T.G. acknowledges financial support from China Scholarship Council and China Postdoctoral Council (PC2022055). M.T. acknowledges a CSH Fellowship of Universität Bern. We thank two journal reviewers who provided constructive comments on earlier versions of the manuscript.

Author affiliations: [a]State Key Laboratory of Environmental Geochemistry, Institute of Geochemistry, Chinese Academy of Sciences, Guiyang 550081, China; [b]Department of Geosciences, Virginia Tech, Blacksburg, VA 24061; [c]Department of Geology, University of Maryland, College Park, MD 20742; [d]College of Earth and Planetary Sciences, University of Chinese Academy of Sciences, Beijing 101408, China; [e]Center for Space and Habitability, University of Bern, Bern 3012, Switzerland; [f]University Observatory Munich, Faculty of Physics, Ludwig Maximilian University, Munich D-81679, Germany; [g]Department of Earth, Marine and Environmental Sciences, University of North Carolina, Chapel Hill 27599, NC; [h]Department of Geoscience, University of Nevada, Las Vegas, NV 89154; [i]Department of Earth and Environmental Sciences, Denison University, Granville, OH 24060; [j]Earth System Science Interdisciplinary Center, University of Maryland, College Park, MD 20742; and [k]State Key Laboratory of Ore Deposit Geochemistry, Institute of Geochemistry, Chinese Academy of Sciences, Guiyang 550081, China

Author contributions: T.G., M.T., and S.X. designed research; T.G., M.T., X.-K.W., and S.X. performed research; T.G., M.T., X.-K.W., S.W., X.-M.L., G.J., B.C.G., M.N., A.J.K., T.L., and S.X. contributed new reagents/analytic tools; T.G., M.T., X.-M.L., and S.X. analyzed data; and T.G., M.T., X.-M.L., G.J., A.J.K., and S.X. wrote the paper.

1. P. F. Hoffman, A. J. Kaufman, G. P. Halverson, D. P. Schrag, A Neoproterozoic snowball Earth. *Science* **281**, 1342–1346 (1998).
2. P. F. Hoffman *et al.*, Snowball Earth climate dynamics and Cryogenian geology-geobiology. *Sci. Adv.* **3**, e1600983 (2017).
3. M. J. Kennedy, B. Runnegar, A. R. Prave, K. H. Hoffmann, M. A. Arthur, Two or four Neoproterozoic glaciations. *Geology* **26**, 1059–1063 (1998).
4. G. Jiang, M. J. Kennedy, N. Christie-Blick, H. Wu, S. Zhang, Stratigraphy, sedimentary structures, and textures of the late Neoproterozoic Doushantuo cap carbonate in South China. *J. Sediment. Res.* **76**, 978–995 (2006).
5. J. A. Higgins, D. P. Schrag, Aftermath of a snowball Earth. *Geochem. Geophys. Geosyst.* **4**, 1–20 (2003).
6. P. F. Hoffman, D. P. Schrag, The snowball Earth hypothesis: Testing the limits of global change. *Terra Nova* **14**, 129–155 (2002).
7. M. J. Kennedy, N. Christie-Blick, L. E. Sohl, Are Proterozoic cap carbonates and isotopic excursions a record of gas hydrate destabilization following Earth's coldest intervals? *Geology* **29**, 443–446 (2001).
8. G. Jiang, M. J. Kennedy, N. Christieblick, Stable isotopic evidence for methane seeps in Neoproterozoic postglacial cap carbonates. *Nature* **426**, 822–826 (2003).
9. J. P. Grotzinger, A. H. Knoll, Anomalous carbonate precipitates: Is the Precambrian the key to the Permian? *Palaios* **10**, 578–596 (1995).
10. W. Yu *et al.*, Evaluation of alkalinity sources to Cryogenian cap carbonates, and implications for cap carbonate formation models. *Global Planet. Change* **217**, 103949 (2022).
11. G. A. Shields, Neoproterozoic cap carbonates: A critical appraisal of existing models and the plumeworld hypothesis. *Terra Nova* **17**, 299–310 (2005).
12. S. A. Kasemann, C. J. Hawkesworth, A. R. Prave, A. E. Fallick, P. N. Pearson, Boron and calcium isotope composition in Neoproterozoic carbonate rocks from Namibia: Evidence for extreme environmental change. *Earth Planet. Sci. Lett.* **231**, 73–86 (2005).
13. C. Liu, Z. Wang, T. D. Raub, F. A. Macdonald, D. A. D. Evans, Neoproterozoic cap-dolostone deposition in stratified glacial meltwater plume. *Earth Planet. Sci. Lett.* **404**, 22–32 (2014).
14. S. A. Kasemann, A. R. Prave, A. E. Fallick, C. J. Hawkesworth, K.-H. Hoffmann, Neoproterozoic ice ages, boron isotopes, and ocean acidification: Implications for a snowball Earth. *Geology* **38**, 775–778 (2010).
15. J. Yang, M. F. Jansen, F. A. Macdonald, D. S. Abbot, Persistence of a freshwater surface ocean after a snowball Earth. *Geology* **45**, 615–618 (2017).
16. L. Ramme, J. Marotzke, Climate and ocean circulation in the aftermath of a Marinoan snowball Earth. *Climate Past* **18**, 759–774 (2022).
17. P. B. Tomascak, T. Magna, R. Dohmen, *Advances in lithium isotope geochemistry*, J. Hoefs, Ed. (Springer, 2016).
18. S. Penniston-Dorland, X.-M. Liu, R. L. Rudnick, Lithium isotope geochemistry. *Rev. Mineral. Geochem.* **82**, 165–217 (2017).
19. P. A. E. Pogge von Strandmann, H. C. Jenkyns, R. G. Woodfine, Lithium isotope evidence for enhanced weathering during Oceanic Anoxic Event 2. *Nat. Geosci.* **6**, 668–672 (2013).
20. E. Lemarchand, F. Chabaux, N. Vigier, R. Millot, M.-C. Pierret, Lithium isotope systematics in a forested granitic catchment (Strengbach, Vosges Mountains, France). *Geochim. Cosmochim. Acta* **74**, 4612–4628 (2010).
21. W. Li, X.-M. Liu, O. A. Chadwick, Lithium isotope behavior in Hawaiian regoliths: Soil-atmosphere-biosphere exchanges. *Geochim. Cosmochim. Acta* **285**, 175–192 (2020).
22. X.-M. Liu, R. L. Rudnick, W. F. McDonough, M. L. Cummings, Influence of chemical weathering on the composition of the continental crust: Insights from Li and Nd isotopes in bauxite profiles developed on Columbia River Basalts. *Geochim. Cosmochim. Acta* **115**, 73–91 (2013).
23. S. Misra, P. N. Froelich, Lithium isotope history of Cenozoic seawater: Changes in silicate weathering and reverse weathering. *Science* **335**, 818–823 (2012).
24. F. T. Mackenzie, L. R. Kump, Reverse weathering, clay mineral formation, and oceanic element cycles. *Science* **270**, 586–586 (1995).
25. B. Kalderon-Asael *et al.*, A lithium-isotope perspective on the evolution of carbon and silicon cycles. *Nature* **595**, 394–398 (2021).
26. P. A. E. Pogge von Strandmann, S. A. Kasemann, J. B. Wimpenny, Lithium and lithium isotopes in Earth's surface cycles. *Elements* **16**, 253–258 (2020).
27. M. L. Delaney, E. A. Boyle, Lithium in foraminiferal shells: Implications for high-temperature hydrothermal circulation fluxes and oceanic crustal generation rates. *Earth Planet. Sci. Lett.* **80**, 91–105 (1986).
28. M.-L. Siggaard-Andersen, J. P. Steffensen, H. Fischer, Lithium in Greenland ice cores measured by ion chromatography. *Ann. Glaciol.* **35**, 243–249 (2002).
29. C. Zhou, H. Bao, Y. Peng, X. Yuan, Timing the deposition of ^{17}O-depleted barite at the aftermath of Nantuo glacial meltdown in South China. *Geology* **38**, 903–906 (2010).
30. T. Gan *et al.*, Earliest Ediacaran speleothems and their implications for terrestrial life after the Marinoan snowball Earth. *Precambrian Res.* **376**, 1–22 (2022).
31. C. Zhou, X. Lang, M. H. Huyskens, Q. Yin, S. Xiao, Calibrating the terminations of Cryogenian global glaciations. *Geology* **47**, 251–254 (2019).
32. D. Condon *et al.*, U-Pb ages from the neoproterozoic doushantuo formation, China. *Science* **308**, 95–98 (2005).
33. G. Jiang, X. Shi, S. Zhang, Y. Wang, S. Xiao, Stratigraphy and paleogeography of the Ediacaran Doushantuo Formation (ca. 635–551 Ma) in South China. *Gondwana Res.* **19**, 831–849 (2011).
34. H. L. Taylor *et al.*, Lithium isotope composition of Ediacaran dolostones from the Nuccaleena and Doushantuo formations. *Aust. J. Earth Sci.* **70**, 1159–1171 (2023).
35. Y.-S. Yin *et al.*, Widespread clay authigenesis and highly congruent silicate weathering in the Marinoan aftermath. *Earth Planet. Sci. Lett.* **623**, 118423 (2023).
36. C. Liu, Z. Wang, T. D. Raub, Geochemical constraints on the origin of Marinoan cap dolostones from Nuccaleena Formation, South Australia. *Chem. Geol.* **351**, 95–104 (2013).
37. G.-Y. Wei *et al.*, Ca and Sr isotope constraints on the formation of the Marinoan cap dolostones. *Earth Planet. Sci. Lett.* **511**, 202–212 (2019).
38. J. Wang, A. D. Jacobson, B. B. Sageman, M. T. Hurtgen, Application of the $\delta^{44/40}$Ca-$\delta^{88/86}$Sr multi-proxy to Namibian Marinoan cap carbonates. *Geochim. Cosmochim. Acta* **353**, 13–27 (2023).
39. T. F. Bristow *et al.*, Mineralogical constraints on the paleoenvironments of the Ediacaran Doushantuo Formation. *Proc. Natl. Acad. Sci. U.S.A.* **106**, 13190–13195 (2009).
40. S. Han *et al.*, Authigenic clay mineral evidence for restricted, evaporitic conditions during the emergence of the Ediacaran Doushantuo Biota. *Commun. Earth Environ.* **3**, 165 (2022).
41. C. Cao, X.-M. Liu, X.-K. Wang, J. Chen, Effective use of limestones to reconstruct seawater Li isotope compositions - A community standard proposal. *Chem. Geol.* **626**, 121441 (2023).
42. P.-H. Tsai, C.-F. You, K.-F. Huang, C.-H. Chung, Y.-B. Sun, Lithium distribution and isotopic fractionation during chemical weathering and soil formation in a loess profile. *J. Asian Earth Sci.* **87**, 1–10 (2014).
43. P. F. Hoffman *et al.*, Are basal Ediacaran (635 Ma) post-glacial "cap dolostones" diachronous? *Earth Planet. Sci. Lett.* **258**, 114–131 (2007).
44. M. Dellinger *et al.*, The effects of diagenesis on lithium isotope ratios of shallow marine carbonates. *Am. J. Sci.* **320**, 150–184 (2020).
45. M. J. Kennedy, Stratigraphy, sedimentology, and isotopic geochemistry of Australian Neoproterozoic postglacial cap dolostones: Deglaciation, delta C-13 excursions, and carbonate precipitation. *J. Sediment. Res.* **66**, 1050–1064 (1996).
46. W. Hegenberger, Gas escape structures in Precambrian peritidal carbonate rocks. *Commun. Geol. Sur. South West Africa, Namibia* **3**, 49–55 (1987).
47. P. Cloud, L. A. Wright, E. G. Williams, P. Diehl, M. R. Walter, Giant stromatolites and associated vertical tubes from the Upper Proterozoic Noonday Dolomite, Death Valley Region, Eastern California. *Geol. Soc. Am. Bull.* **85**, 1869–1882 (1974).
48. A. Siedlecka, D. Roberts, The bedrock geology of Varanger Peninsula, Finmark, North Norway: An excursion guide. *Geol. Sur. Norway* **45**, 1–45 (1992).
49. C. Vasconcelos, J. A. McKenzie, S. Bernasconi, D. Grujic, A. J. Tiens, Microbial mediation as a possible mechanism for natural dolomite formation at low temperatures. *Nature* **377**, 220–222 (1995).
50. C. V. Rose, A. C. Maloof, Testing models for post-glacial "cap dolostone" deposition: Nuccaleena formation, South Australia. *Earth Planet. Sci. Lett.* **296**, 165–180 (2010).
51. T. D. Raub, *Prolonged deglaciation of "Snowball Earth"* (Yale University, Connecticut, United States, 2008), p. 296.
52. J. G. Murphy, A.-S.C. Ahm, P. K. Swart, J. A. Higgins, Reconstructing the lithium isotopic composition (δ^7Li) of seawater from shallow marine carbonate sediments. *Geochim. Cosmochim. Acta* **337**, 140–154 (2022).
53. T. T. Isson, N. J. Planavsky, Reverse weathering as a long-term stabilizer of marine pH and planetary climate. *Nature* **560**, 471–475 (2018).
54. C. Cao *et al.*, Persistent late Permian to early Triassic warmth linked to enhanced reverse weathering. *Nat. Geosci.* **15**, 832–838 (2022).
55. R. S. Hindshaw *et al.*, Experimental constraints on Li isotope fractionation during clay formation. *Geochim. Cosmochim. Acta* **250**, 219–237 (2019).
56. J. S. Pistiner, G. M. Henderson, Lithium-isotope fractionation during continental weathering processes. *Earth Planet. Sci. Lett.* **214**, 327–339 (2003).
57. X.-F. Liu, X.-M. Liu, X.-K. Wang, S. Zhai, X. Liu, Dolostone as a reliable tracer of seawater lithium isotope composition. *Commun. Earth Environ.* **4**, 58 (2023).
58. C. S. Marriott, G. M. Henderson, N. S. Belshaw, A. W. Tudhope, Temperature dependence of δ^7Li, δ^{44}Ca and Li/Ca during growth of calcium carbonate. *Earth Planet. Sci. Lett.* **222**, 615–624 (2004).
59. A. Füger *et al.*, Effect of growth rate and pH on Li isotope fractionation during its incorporation in calcite. *Geochim. Cosmochim. Acta* **323**, 276–290 (2022).
60. C. S. Marriott, G. M. Henderson, R. Crompton, M. Staubwasser, S. Shaw, Effect of mineralogy, salinity, and temperature on Li/Ca and Li isotope composition of calcium carbonate. *Chem. Geol.* **212**, 5–15 (2004).
61. M. Tian, T. Gan, S. Xiao (2024) Mass Balance Box Model for Lithium Isotope Evolution in Seawater. Zenodo. https://doi.org/10.5281/zenodo.13924312.
62. B. Bodiselitsch, C. Koeberl, S. Master, W. U. Reimold, Estimating duration and intensity of Neoproterozoic snowball glaciations from Ir anomalies. *Science* **308**, 239–242 (2005).
63. J. Korenaga, Initiation and evolution of plate tectonics on Earth: Theories and observations. *Annu. Rev. Earth Planet. Sci.* **41**, 117–151 (2013).
64. C. O'Neill, A. Lenardic, T. Höink, N. Coltice, "Mantle convection and outgassing on terrestrial planets" in *Comparative Climatology of Terrestrial Planets*, S. J. Mackwell, A. A. Simon-Miller, J. W. Harder, M. A. Bullock, Eds. (University of Arizona, Tucson, 2014), pp. 473–486.

65. P. A. E. Pogge von Strandmann *et al.*, Lithium isotopes in speleothems: Temperature-controlled variation in silicate weathering during glacial cycles. *Earth Planet. Sci. Lett.* **469**, 64–74 (2017).
66. G. Li, A. J. West, Evolution of Cenozoic seawater lithium isotopes: Coupling of global denudation regime and shifting seawater sinks. *Earth Planet. Sci. Lett.* **401**, 284–293 (2014).
67. X.-M. Liu, W. Li, Optimization of lithium isotope analysis in geological materials by quadrupole ICP-MS. *J. Anal. At. Spectrom.* **34**, 1708–1717 (2019).
68. W. Li, X.-M. Liu, L. V. Godfrey, Optimisation of lithium chromatography for isotopic analysis in geological reference materials by MC-ICP-MS. *Geostand. Geoanal. Res.* **43**, 261–276 (2019).
69. S. C. Penniston-Dorland, G. E. Bebout, P. A. E. Pogge von Strandmann, T. Elliott, S. S. Sorensen, Lithium and its isotopes as tracers of subduction zone fluids and metasomatic processes: Evidence from the Catalina Schist, California, USA. *Geochim. Cosmochim. Acta* **77**, 530–545 (2012).
70. C. Cao, X.-M. Liu, C. P. Bataille, C. Liu, What do Ce anomalies in marine carbonates really mean? A perspective from leaching experiments *Chem. Geol.* **532**, 119413 (2020).